Geomechanics and Engineering, *Vol. 22, No. 2 (2020) 187-196*
DOI: https://doi.org/10.12989/gae.2020.22.2.187

Waveform characterization and energy dissipation of stress wave in sandstone based on modified SHPB tests

Yun Cheng*[1], Zhanping Song[1,2a], Jiefang Jin[3b], Tong Wang[1,2] and Tengtian Yang[2,4]

[1]School of Civil Engineering, Xi'an University of Architecture and Technology, Xi'an 710055, China
[2]Shaanxi Key Laboratory of Geotechnical and Underground Space Engineering, Xi'an 710055, China
[3]School of Architectural and Surveying Engineering, Jiangxi University of Science and Technology, Ganzhou 341000, China
[4]China Railway Bridge Engineering Bureau Group Co. Ltd., Tianjin 300300, China

(Received March 29, 2019, Revised May 28, 2020, Accepted June 22, 2020)

Abstract. The changeable stress environment directly affect the propagation law of a stress wave. Stress wave propagation tests in sandstone with different axial stresses were carried using a modified split Hopkinson Pressure bar (SHPB) assuming the sandstone has a uniform pore distribution. Then the waveform and stress wave energy dissipation were analyzed. The results show that the stress wave exhibits the double peak phenomenon. With increasing axial stress, the intensity difference decreases exponentially and experiences first a dramatic decrease and then gentle development. The demarcation stress is σ/σ_c=30%, indicating that the closer to the incident end, the faster the intensity difference attenuates. Under the same axial stress, the intensity difference decreases linearly with propagation distance and its attenuation intensity factor displays a quadratic function with axial stress. With increasing propagation distance, the time difference decays linearly and its delay coefficient reflects the damage degree. The stress wave energy attenuates exponentially with propagation distance, and the relations between attenuation rate, attenuation coefficient and axial stress can be represented by the quadratic function.

Keywords: sandstone; axial stress; stress wave; waveform characterization

1. Introduction

Recently, many underground engineering and infrastructure projects, such as urban metro systems, mountain tunnel, and mining structures, have been constructed in China (Wu and Shao 2019a, b). Therefore, it is inevitable that mechanical drilling and blasting in rock masses is required to damage the rock mass (Tian *et al.* 2019, Fan *et al.* 2020). The subsequent stress wave produced by these construction activities will induce instability and possible failure of engineering rock masses (Wang *et al.* 2019a, Song *et al.* 2018). Simultaneously, excavation behaviors not only destroy the balance of the original stress in rock masses, but they also lead to the redistribution of the initial stress, resulting in the rock mass existing in a new stress environment (Li *et al.* 2005, Nikadat and Marji 2016). Additionally, a stress wave propagating through a natural rock mass is a complex physical process, and the changeable mechanical environment may change the transmission and reflection capability of the stress wave in the pores and joints. This further increases the complexity of exploring the propagation characteristics of stress waves in rock mass. Therefore, it is of great significance to study stress wave propagation in rock masses under different static stress conditions for the construction and operation safety of rock mass engineering.

The propagation and attenuation characteristics of a stress wave in a rock mass have been concerned in geotechnical engineering. However, a unified quantitative relationship has not been found to demonstrate the propagation characteristic of a stress wave due to the complexity and discontinuity of rock masses. In addition to the necessary physical, mechanical properties and geological factors, changes in porosity will directly lead to a change in stress wave velocity, amplitude, and energy (Ju *et al.* 2006, Cheng *et al.* 2019). The influence of dynamic and static loads on dynamic characteristics during blasting excavation of deep rock masses, and these studies can be divided into the dynamic response and stress wave propagation. The impact tests of rock samples with a ratio of length to diameter of less than one have primarily been conducted using a split Hopkinson pressure bar (SHPB), initially developed by Kolsky (1949), or a developed SHPB. This research method has been widely used and improved with the continuous development of impact dynamics (Li *et al.* 2005). As shown in a previous analysis, an excavated rock mass is typically in a specific static stress environment, and static stress affects the initial porosity or damage degree, and the dynamic mechanical response varies significantly (Ju *et al.* 2006, Khosravani *et al.* 2019a, b). When the impact strength, impact times, and axial stress of the rock are different, the breaking characteristics and

*Corresponding author, Ph.D. Candidate
E-mail: chengyun_ifu@163.com
[a]Professor, Ph.D.
E-mail: songzhpyt@xauat.edu.cn
[b]Professor, Ph.D.
E-mail: jjf_chang@126.com

Copyright © 2020 Techno-Press, Ltd.
http://www.techno-press.org/?journal=gae&subpage=7
ISSN: 2005-307X (Print), 2092-6219 (Online)

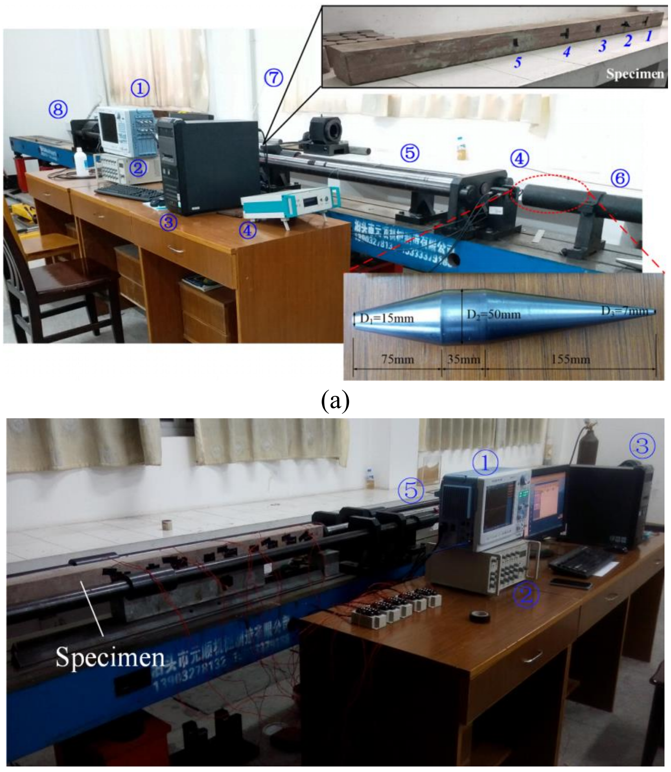

Fig. 1 The modified SHPB (Cheng *et al.* 2019): ① oscillograph, ② dynamic strain meter, ③ computer, ④ laser velocimeter device, ⑤ incident bar, ⑥ striker bar chamber, ⑦ specimen, ⑧ stress loading device; 1, 2, 3, 4 and 5 represent the test points

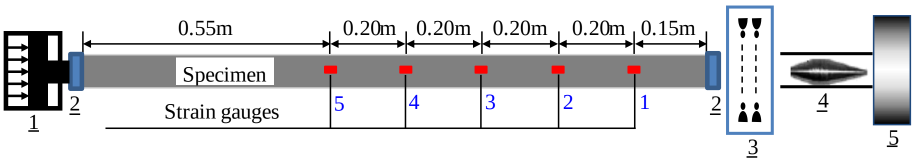

Fig. 2 Diagram of the modified SHPB: 1. stress loading device, 2. steel pads, 3. laser velocimeter device, 4. striker bar, 5. high-pressure air chamber. 1, 2, 3, 4 and 5 represent the test points, corresponding to the test points on the specimen in Fig. 1

energy dissipation laws are very different (Li *et al.* 2005, Wang *et al.* 2019b). Therefore, it is of great significance to study the effect of a rock stress environment and external impact conditions on the rock dynamic response to improve the impact resistance, stability or excavation efficiency of a rock mass. For the stress wave propagation in the large-size rock sample, Li *et al.* (2010), and Fan *et al.* (2011) also paid attention to this problem and carried out experimental research. Nevertheless, it can be seen that those samples are all pieced together and not whole pieces. Due to extremely instability of the spliced rock samples, the above studies failed to reveal the stress wave propagation and energy dissipation principles under different stress conditions.

Moreover, stress wave propagation is a process of energy consumption, its variation characteristics of amplitude, transmission and reflection capacity, and energy dissipation also relate to the physical properties of a rock mass, such as porosity, pore geometry size, and pore distribution (Huang *et al.* 2017). Fan and Sun (2015) applied the displacement discontinuity method to study the effect of original rock stress on stress wave propagation in a rock mass with different amplitudes and frequencies. Aliabadian *et al.* (2014) discussed the deformation and fracture behaviors of rock specimens under impact loads in conjunction, and analyzed the waveform of the incident wave. Yoshida *et al.* (2019) conducted stress wave propagation tests on pumice-stone and granite samples using SHPB under high-speed impact and discussed the waveform and time difference between the rises of the incident and transmitted waves. The previous studies have paid more attention to the dynamic response of rock, and they have obtained rich results that can provide technical guidance for practical engineering. However, those studies of the characteristics of stress wave propagation in a rock mass are not enough, especially for the stress wave propagation during the process of the entire rock mass deformation under static stress.

In this study, the length of the incident and transmission bar of the SHPB was reduced, and then multiple strain gauges were pasted on a sandstone bar to obtain the stress wave signal under the entire strain condition. Then, stress wave propagation experiments were conducted on the sandstone using a fixed impact speed utilizing the modified SHPB. Then the stress wave signals were obtained using different axial stresses. The experimental data were analyzed from the viewpoints of: (i) the double peak characteristics of stress wave, including the effect of axial stress on the intensity difference and time difference; (ii) the theoretical analysis of stress wave energy; and (iii) the energy dissipation characteristics of stress wave, including the effect of axial stress on the decline rate and attenuation coefficient. The results of this study can provide a theoretical reference for rock mass stability analyses during blasting excavations.

2. Experiment and specimen

2.1 Apparatus

The modified SHPB test device in the impact mechanics laboratory of Jiangxi University of Science and Technology can provide both axial stress and stress wave, as shown in Figs. 1 and 2. This test device is composed of an axial stress loading device, a dynamic loading device (striker bar and striker bar chamber), a laser velocimeter device (JXCS-02 made in China), a data acquisition device (SDY2017A dynamic strain meter made in Japan), and a data display device (Yokowaga DL850E oscillograph made in Japan). The striker bar of the dynamic loading device is spindle-type that can load a half-sine wave and eliminate PC oscillation. The sampling time ranges from -0.10 ms to 0.90 ms and can collect 1000 time points.

2.2 Sandstone material

2.2.1 Uniaxial compressive strength σ_c of sandstone

The sandstone material used in the stress wave propagation test is obtained from the Huaping Quarry in Ganzhou (China). The red sandstone has good integrity and homogeneity. The density and particle size are 2.35 g/cm^3, and 0.05~2.00 mm, respectively. The stress-strain curve of the standard sandstone (Φ50 mm × 100 mm) is tested using a RMT-150C rock mechanical test machine (made in China), as shown in Fig. 3. This test result indicates that the failure process experiences that occurred during the compaction stage, the elastic deformation stage, the cracks development, expansion stage, and the failure stage. The uniaxial compressive strength (σ_c) and elastic modulus (E) are 52.00 MPa and 5.65 GPa, respectively.

2.2.2 Maximum loading stress of specimen

Due to having to arrange multiple signal points on the specimen to measure the data set, and also since the brittle failure characteristic, the sandstone is processed into a sandstone bar with a section of 80 mm × 80 mm and a length of 1500 mm after the exploration tests.

Then, to reasonably set the stress loading range, the tentative experiment shows that the maximum loading stress (σ_{max}) of the sandstone bar (Fig. 2) for the dynamic test is approximately 39.00 MPa (the critical stress of instability), which is 75% of the uniaxial compressive strength (σ_c). The failure specimen in the tentative experiment, as shown in Fig. 4.

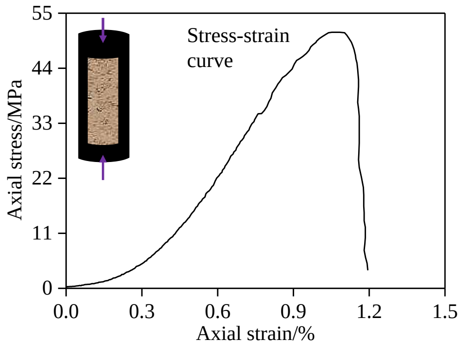

Fig. 3 Stress-strain curve (Cheng *et al.* 2019)

Fig. 4 Failure specimen

2.2.3 Loading range of axial stress

Since the axial stresses loaded to specimen are provided by an hydraulic pump (stress loading device), its values (σ_n) are set to 0, 1, 2, 3, 4, …, 10, 11 and 12 MPa. Then, the axial stress (σ) of the specimen is obtained according to the equation $\sigma = 2.76\sigma_n$, where $S_1/S_2 \approx 2.76$ is the cross-sectional area ratio of hydraulic pump piston to the specimen. The corresponding axial stresses (σ) are 0, 2.76 MPa, 5.52 MPa, 8.28 MPa, 11.04 MPa, ... , 27.60 MPa, 30.36 MPa, 33.12 MPa.

The previous study (Li *et al.* 2005) has shown that when the stress wave amplitude is less than 60% of the rock static strength under a cycling stress wave, the damage caused by the cyclic stress wave can be ignored. Based on this, the cyclic stress wave amplitude in this test is confirmed using an explorative analyses. The striker bar hit the incident bar at a velocity of approximately 4.38 m/s, and the stress wave generated is a type of half-sine wave. The impact velocity is measured using a laser velocimeter.

2.3 Test procedures

To obtain the stress wave signal under different axial stress conditions, the following test principles and procedures of the designed tests are performed.

The specimen is assembled using the modified SHPB, and the steel pads, each with an area slightly larger than the cross-section of the specimen, are added to the interfaces

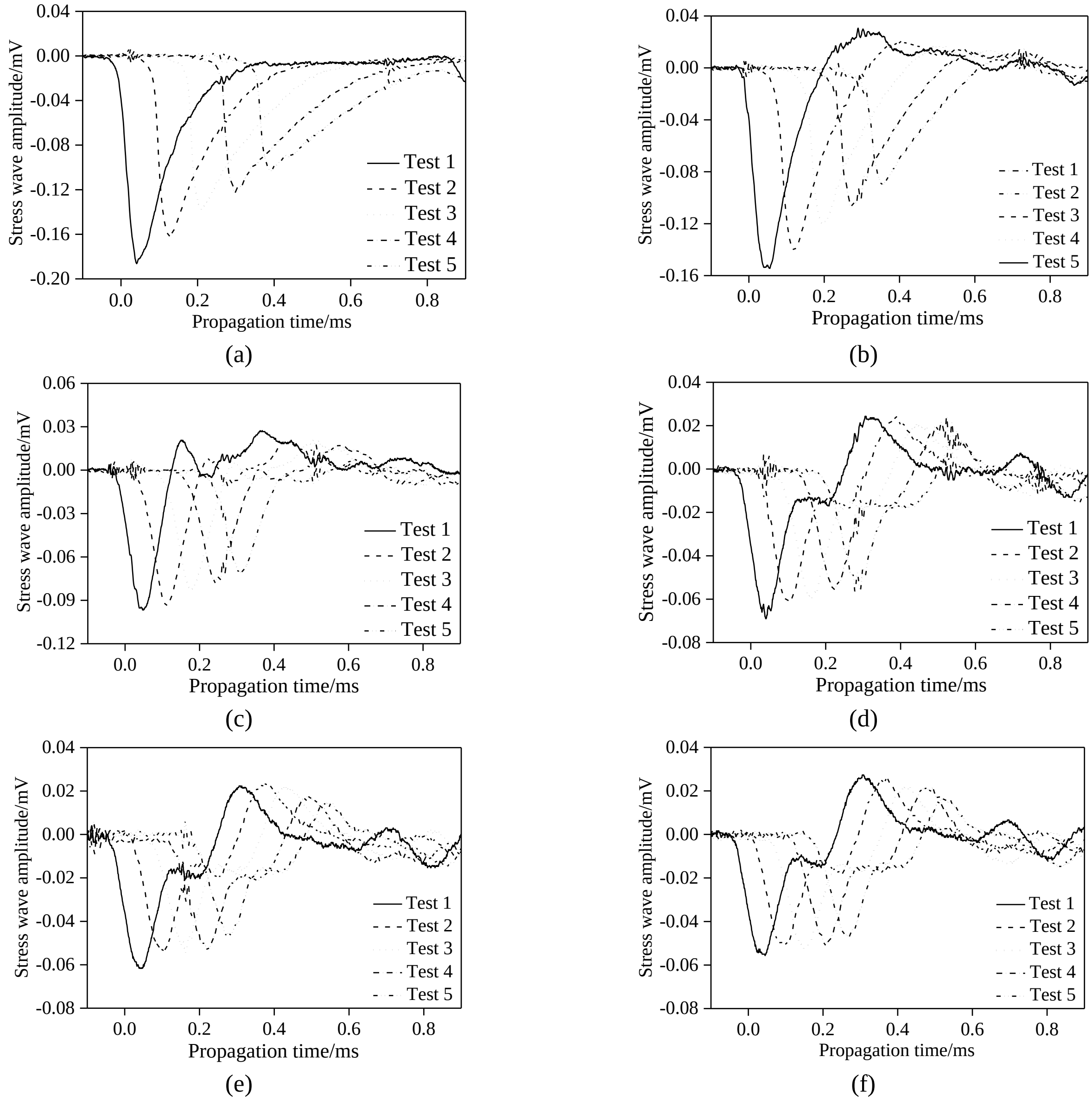

Fig. 5 Waveforms under different axial stresses. (a) 0, (b) 2.76 MPa, (c) 8.28 MPa, (d) 16.56 MPa, (e) 24.84 MPa and (f) 32.12 MPa

between the specimen and the incident bar, transmission bar to prevent the occurrence of a stress concentration phenomenon. In addition, the coupling agents (mechanical butter) is smeared on both sides of the steel pads to reduce the inter-facial friction to ensure the excellent transmission of stress wave signals.

The test points are arranged on the specimen surface. There are five test points on the specimen surface, which are called the test points 1, 2, 3, 4, and 5. Two longitudinally symmetric strain gauges are attached to each test point to lower the test error. Fig. 2 shows the location and spacing of the five test points.

Three impact tests of the same strength under each axial stress are carried, and then the stress wave signals under different axial stresses are saved. The propagation path of the stress wave is the incident end of the specimen, data acquisition device (dynamic strain gauge), data display device (oscilloscope), and data storage device (computer). All of the stress wave propagation tests are completed in this way.

3. Results and discussion

3.1 Double peak characteristics of stress wave

In this study, waveforms with 13 different axial stresses are tested using the modified SHPB. Due to a large number of experimental data, only the waveforms of 0 MPa, 2.76 MPa, 8.28 MPa, 16.56 MPa, 24.84 MPa, and 33.13 MPa are shown in Fig. 5. The stress wave amplitudes are characterized by the measured voltage values (mV), and the positive and negative ordinate values indicate the tensile wave and compression wave, respectively.

The effect of axial stress on stress wave propagation with propagation time, especially on the waveform, is

Table 1 The intensity difference and time difference of double peak

Axial stress /MPa	Intensity difference ΔA_n /mV					Time difference ΔT_n /ms				
	Test 1	Test 2	Test 3	Test 4	Test 5	Test 1	Test 2	Test 3	Test 4	Test 5
0.00	0.1863	0.1620	0.1377	0.1230	0.1033	0.3290	0.3840	0.4070	0.4630	0.5070
2.76	0.1850	0.1610	0.1367	0.1130	0.0997	0.3200	0.3670	0.3900	0.4280	0.4940
5.52	0.1635	0.1410	0.1197	0.1153	0.0923	0.3120	0.3200	0.3480	0.3880	0.4450
8.28	0.1240	0.1140	0.1037	0.0957	0.0797	0.3060	0.3210	0.3320	0.3660	0.4050
11.04	0.1117	0.1020	0.0947	0.0887	0.0744	0.2980	0.3030	0.3130	0.3480	0.3870
13.80	0.0977	0.0910	0.0850	0.0797	0.0700	0.3000	0.2960	0.2890	0.2960	0.3790
16.56	0.0800	0.0717	0.0933	0.0853	0.0807	0.2900	0.2950	0.2950	0.2980	0.3700
19.32	0.0903	0.0833	0.0797	0.0760	0.0670	0.2830	0.2900	0.3000	0.3170	0.3710
22.08	0.0897	0.0850	0.0800	0.0783	0.0667	0.2780	0.2950	0.2880	0.3000	0.3300
24.84	0.0839	0.0783	0.0767	0.0719	0.0613	0.2700	0.2720	0.2700	0.2900	0.3190
27.60	0.0851	0.0780	0.0743	0.0767	0.0620	0.2620	0.2700	0.2730	0.3000	0.3290
30.36	0.0853	0.0793	0.0777	0.0746	0.0653	0.2600	0.2690	0.2790	0.3100	0.3390
33.12	0.0830	0.0770	0.0750	0.0730	0.0637	0.2480	0.2630	0.2840	0.3390	0.3980

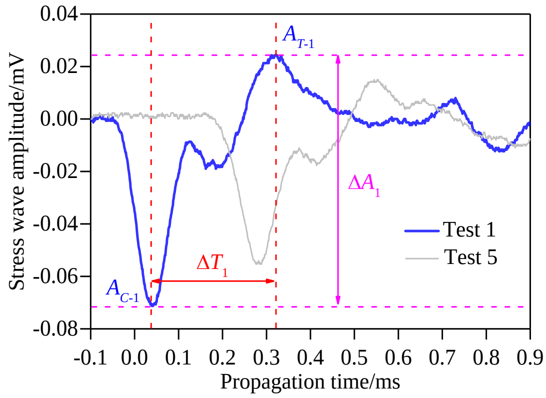

Fig. 6 Diagram of double peak phenomenon

shown in Fig. 5. These figures illustrate that the presence or absence of axial stress in the sandstone has a significant effect on the waveform characteristics. When there is no axial stress in Fig. 5(a), only the compression wave exists and nearly no tensile wave. This is due to the primary pores present in the specimen and the lack of secondary pores, and the reflection phenomenon of the stress wave in pore interface is not apparent. When the axial stress is more than 0 MPa in Figs. 5(b-f), the tensile wave appears in the tail of the stress wave at each test point. In addition, the larger the axial stress, the more obvious the tensile amplitude that occurrence. The reason is that the increased axial stress results in the closure, and initiation of pores in the specimen, and the number of total pores tends to increase, leading to an aggravation of the reflection phenomenon of the stress waves (the compression wave reflects into a tensile wave at the pore interface). However, when stress waves including compression wave and tensile wave with different properties propagate in a rock, the rock will be subjected to the interaction effect of the compressive stress and the tensile stress, and spallation failure will be induced when the mechanical damage reaches an individual strength. Due to the stress restraint effect of specimen ends, the spallation failure is not apparent in this study.

Moreover, when the specimen has the same axial stress, the waveforms in the different locations have a similar development tendency. However, the stress wave amplitude shows an attenuation trend with an increase in propagation distance. With increasing axial stress, the stress wave in the sandstone gradually shows a double peak characteristic. This means that there is a coexistence phenomenon of a compression wave peak and a tensile wave peak. By using Fig. 6 (11.04 MPa) as an example, with increases in propagation time, the stress wave first "jumps" along the negative direction of the longitudinal axis to reach a compression wave peak $A_{C\text{-}1}$, and then the stress wave "climbs" to form a tensile wave peak $A_{T\text{-}1}$ after propagation time ΔT_1 (here, C and T denote the compression wave, tensile wave, respectively). This shows that the existence of axial stress has a significant effect on the formation of the tensile wave. The reason is that the increased axial stress affects the porosity evolution, such as the closure of primary pores, and the initiation and expansion of new pores. This results in different damage degrees and changes the transmission capacity of the specimen.

Figs. 5 and 6 show that the variation characteristic of the waveform primarily reflects in the intensity difference and time difference of the double peak (hereinafter respectively refers to as intensity difference and time difference). Then, the intensity differences and time differences of double peak at the different test points are calculated based on the relationships of $\Delta A_n = A_{C\text{-}n} - A_{T\text{-}n}$ and $\Delta T_n = T_{C\text{-}n} - T_{T\text{-}n}$, as shown in Table 1. The effect of axial stress on the intensity difference and time difference of double peak is discussed in the next sections.

3.2 Intensity difference

3.2.1 Effect of axial stress on intensity difference

Table 1 shows that the double peak intensity difference of the stress wave decreases with increasing axial stress and propagation distance; however, it has different attenuation

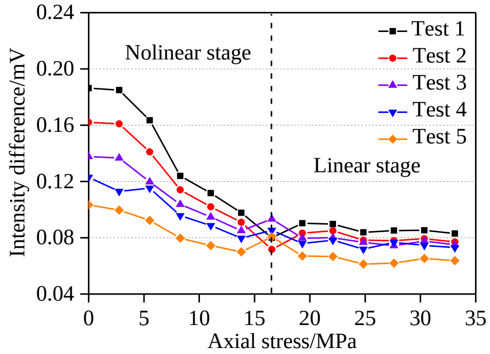

Fig. 7 Variation tendency of intensity difference

Table 2 Regression equation between intensity difference and axial stress

Test points	Regression equation	R^2
Test 1	$\Delta A_1=0.1263e^{-0.1021\sigma}+0.0742$	0.9079
Test 2	$\Delta A_2=0.1037e^{-0.1001\sigma}+0.0697$	0.9328
Test 3	$\Delta A_3=0.0748e^{-0.0868\sigma}+0.0691$	0.9382
Test 4	$\Delta A_4=0.0575e^{-0.0857\sigma}+0.0685$	0.9377
Test 5	$\Delta A_5=0.0477e^{-0.0832\sigma}+0.0593$	0.9086

intensity under different axial stresses. Fig. 7 shows the variation tendency of the intensity difference with different axial stresses at the various locations, which reveals that with increasing axial stress, the intensity difference undergoes first a dramatic decrease (nonlinear stage), then tended to a gentle development (linear stage).

In this study, the stress rate σ/σ_c of axial stress of the specimen to uniaxial compressive strength of the standard sandstone is used to represent the curve demarcation point in Fig. 7. It is found that the demarcation points of the axial stress (hereinafter refers to as the demarcation stress) in the two stages is σ/σ_c=30%. When the stress rate is less than σ/σ_c=30%, the closer to the incident end, the higher the attenuation degree of the intensity difference. When the stress rate is more than σ/σ_c=30%, the intensity difference has a gentle development. The reasons for this are that the collected stress wave signals are mainly broadband waves consisting of different frequencies and at different attenuation levels. It is generally believed that the attenuation intensities of high frequency waves are higher than those of low frequency waves (Pyrak-Nolte 1996). The high frequency waves are absorbed through pores or damage in the sandstone, and the relatively fewer high frequency stress waves are intercepted at the later test points, resulting in a decreased intensity difference.

In addition, a regression analysis reveals that the intensity difference decreases as a first order exponential function with increasing axial stress, and the regression equation and its parameters of the intensity difference are shown in Table 2. Consistent with previous results, the attenuation coefficient (α=0.1021, 0.1001, 0.0868 and 0.0857) in the regression equation decreases gradually with an increase in the propagation distance. This indicates that the closer to the incident bar, the faster the attenuation degree of the intensity difference. This also suggests that

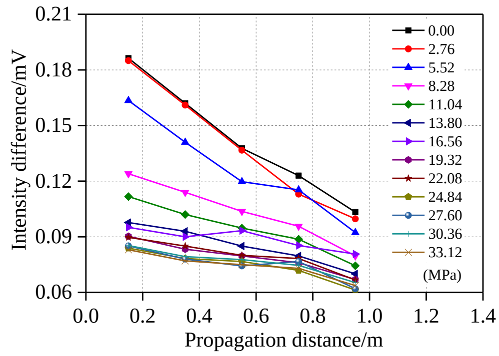

Fig. 8 Variation tendency of intensity difference under different axial stresses

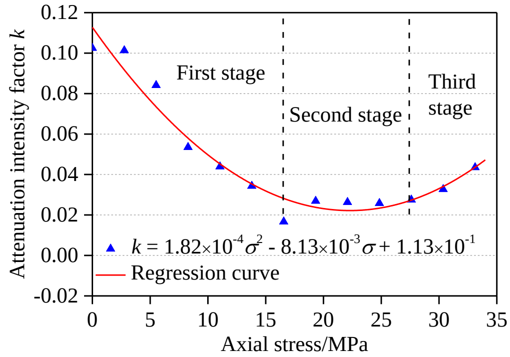

Fig. 9 Relationship between attenuation intensity factor and axial stress

the sandstone under different axial stresses has a filtering effect (Davies and Hunter 1963) on high frequency waves with a varying degree.

3.2.2 Attenuation characteristics of intensity difference

Fig. 8 shows the variation tendency of intensity difference under different axial stresses, and it demonstrates the effect of different axial stresses on attenuation characteristics of intensity difference. It is worth noting that the increase in the propagation distance decreases the intensity difference with different decline degrees, and there exists good linear relationships between the intensity difference and the propagation distance. Here, the linear slopes k of the regression curves are used to describe the attenuation intensity factor of the intensity difference with the propagation distance, and the relationship between attenuation intensity factor and axial stress is shown in Fig. 9.

Fig. 9 shows that the axial stress has a remarkable influence on the attenuation intensity factor k. When the axial stress increases, the attenuation intensity factor k experiences first a dramatic decrease, then smooth development, and finally a sharp increase, and its variation scope is between 0.0167 and 0.1025. The demarcation stresses of the three stages are σ/σ_c=30%, and σ/σ_c=55%, respectively. This is consistent with the variation trend of the attenuation coefficient of stress wave amplitude with increasing static stress (Cheng *et al.* 2019). The laws of pore or damage evolution for sandstone are analyzed as follows.

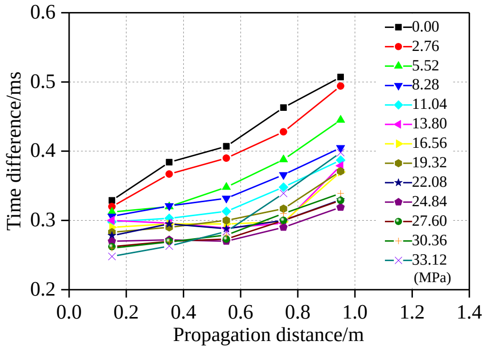

Fig. 10 Variation tendency of time difference under different axial stresses

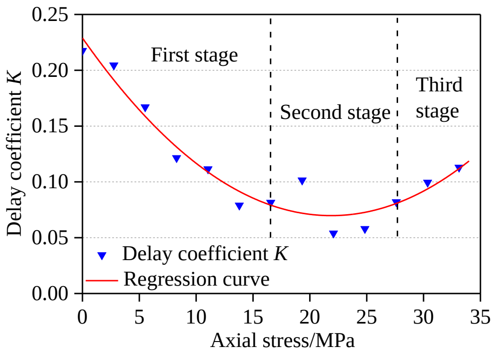

Fig. 11 Relationship between delay coefficient and axial stress

The first stage, when the stress ratio σ/σ_c is less than 30%, the attenuation intensity factor k decreases from 0.1025 to 0.0167, with an 87.80% attenuation. The reason is that the primary pores in the specimen are compacted, and the porosity decreases with increasing axial stress and then weaken the stress wave energy. The first stage can be called the stress strengthening stage.

The second stage, when the stress ratio σ/σ_c is more than 30% and less than 55%, the attenuation intensity factor k displays a gentle development with increasing axial stress, and gradually converges to 0.0260. The reason is due to the coexistence phenomenon of closed pores and newly formed pores caused by the loading stress of the specimen. However, when the number of closed pores is approximately equal to that of new ones, the porosity varies little. The second stage is called the damage development stage.

The third stage, when the stress ratio σ/σ_c is more than 50%, the attenuation intensity factor k increases from 0.0275 to 0.0437, an increase of 58.18%. With an increase in axial stress, the number of newly formed pores increases obviously, and this is accompanied by the initiation and propagation of new micro-cracks. This results in a sharp increase in the internal damage degree. Then, the new pores and micro-cracks gradually dominate the evolution of porosity, thus causing a sharp rise in the attenuation intensity factor k. The third stage is called the failure stage of the specimen.

As the previous analysis, the calculated attenuation intensity factor k of the intensity difference has a different sensitivity to different axial stress ranges, and the relationship (in Fig. 9) between the attenuation intensity factor k and axial stress can be described as a quadratic function (R^2=0.9088).

3.3 Effect of axial stress on time difference

With an increase in the propagation distance, the double peak time difference increases gradually, having a different variation tend with the intensity difference, as shown in Fig. 10. Regression analysis reveals that there are good linear relationships between the time differences and propagation distances, expressing as $\Delta T=Kx+R$, where K and R denote the regression parameters relates to the axial stress. K indicates the growth rate of the time difference with propagation distance, which is called the delay coefficient (Wang *et al.* 2010) in this study.

Fig. 11 shows the variation tendency of the delay coefficient K with increasing axial stress, and the delay coefficient K undergoes first a rapid attenuation, then a stable development, and finally a drastic increase. The demarcation stresses of the three stages, respectively, are σ/σ_c=30%, and σ/σ_c=55%, which is consistent with Fig. 9. This suggests that the variation trend of delay coefficient K can reflect the damage evolution in the specimen to some certain extent. The relationship between the delay coefficient K and axial stress can be described as a quadratic function (R^2=0.9018).

$$K = 3.0\times10^{-6}\sigma^2 + 2.0\times10^{-4}\sigma + 2.25\times10^{-1} \tag{1}$$

3.4 Energy dissipation characteristics of stress wave

3.4.1 Energy dissipation theory

The stress wave attenuation and waveform variation during axial stress loading comprise the energy dissipation of stress wave. The stress wave energy can be represented using the square of stress wave signal (voltage) to reveal the damage evolution of sandstone material. In this study, it is assumed that the stress wave energy is the sum of the compression wave energy and the tensile wave energy, and the stress wave energy can be expressed as Eq. (2).

$$E = \sum_{i=1}^{n} V_n^2 \tag{2}$$

where E is stress wave energy (mV^2), and V_n is voltage amplitude (mV) at time n. The decline rate and the attenuation coefficient of stress wave energy at different locations are discussed as follows.

(1) Decline rate of stress wave energy

Assuming that the stress wave propagates from test point 1 to test point 5, the decline rate of stress wave energy V (mV/m), can be expressed as Eq. (3).

$$V = \frac{E_5 - E_1}{x_5 - x_1} \tag{3}$$

where E_1 and E_5 are the stress wave energy at locations x_1 and x_5, respectively.

(1) Attenuation coefficient of stress wave energy

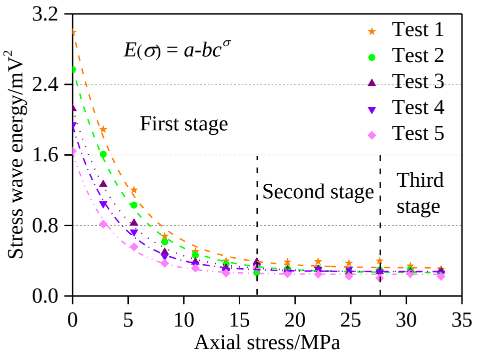

Fig. 12 Attenuation tendency of stress wave energy in different test points

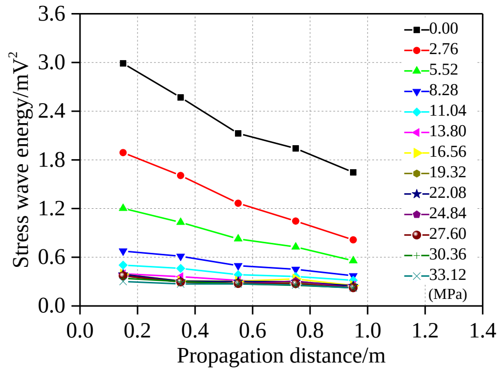

Fig. 13 Variation tendency of stress wave energy under different axial stresses

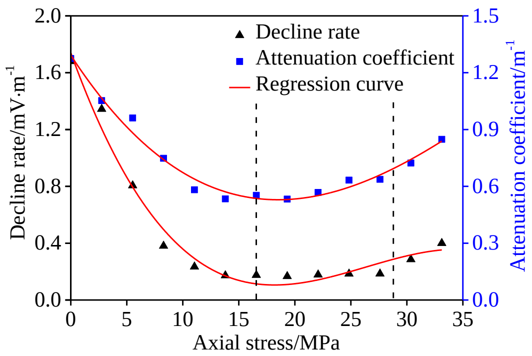

Fig. 14 Variation tendency of decline rate, attenuation coefficient with increasing axial stress

The relative variation of the stress wave energy when the stress wave propagates from location x to $x+\Delta x$ can be expressed as Eq. (4).

$$\frac{E(x+\Delta x) - E(\Delta x)}{E(x)} = -\alpha \Delta x \tag{4}$$

where $E(x)$ and $E(x+\Delta x)$ are the stress wave energy at locations x and $x+\Delta x$, respectively. Eq. (4) shows that the relative variation of the stress wave energy is proportional to Δx, and the proportional coefficient $-\alpha_x$ expresses the spatial attenuation characteristics with increasing propagation distance. If $\Delta x \to 0$, Eq. (4) can be written as Eq. (5).

$$\frac{dE(x)}{dx} = -\alpha E(x) \tag{5}$$

$E(x)$ can be obtained after solving the differential Eq. (5) and is expressed as Eq. (6).

$$E(x) = E_0 e^{-\alpha x} \tag{6}$$

where E_0 denotes the initial energy of the incident wave in sandstone. Eq. (6) shows that the stress wave energy decays exponentially with increasing propagation distance, and the attenuation degree relates to the attenuation coefficient α. In this study, when the stress wave propagates from location x_1 to location x_5 ($x_1 < x_5$), the attenuation coefficient α of the stress wave energy is approximately expressed as Eq. (7).

$$\alpha = -\frac{\ln\left[E(x_1)/E(x_5)\right]}{x_1 - x_5} \tag{7}$$

3.4.2 Effect of axial stress on stress wave energy

Fig. 12 presents the variation tendency of stress wave energy with an increase in the axial stress at different locations calculated using Eq. (2). The development tendency illustrates that the stress wave energy underwent first a dramatic decrease, then gentle development, and finally a gradual decrease. The demarcation stresses of the three stages are σ/σ_c=30%, and σ/σ_c=55%, respectively. When the stress rate σ/σ_c is less than 30%, the stress wave energy shows a noticeable attenuation when the stress wave propagates from test 1 to test 5, and it is decreased by 88.88%, 87.99%, 85.61%, 82.81%, and 82.68%, respectively, at each test point. When the stress rate σ/σ_c is greater than 30% and less than 55%, the decrement of the stress wave energy is between 10.56% and 13.88%. However, when the stress rate σ/σ_c is greater than 55%, the decrement of stress wave energy is less than 10%. This indicates that the stress wave energy has different attenuation sensitives to different loading ranges of the axial stress.

Additionally, the regression relationships between the stress wave energy and axial stress show that the attenuation strength of the stress wave energy is gradually reduced as the propagation distance increases under the same axial stress, which is consistent with Wang *et al.* (2010) and Jin *et al.* (2017). The above phenomena can be explained by the theory of one-dimensional elastic wave (Lifshitz 1994). The regression relationship between the stress wave energy and axial stress can be described as Eq. (8).

$$E(x,\sigma) = \varpi + \xi \lambda^{\sigma} \tag{8}$$

where $E(x, \sigma)$ denotes the stress wave energy, and its value relates to the propagation distance x and the axial stress σ; ϖ, ξ and λ denote the regression parameters relate to the propagation distance x, where

$$\varpi = 8.42\times10^{-2}x + 8.32\times10^{-1}, \quad \xi = -1.66x + 2.90,$$
$$\lambda = 6.50\times10^{-2}x + 3.12\times10^{-1}.$$

3.4.3 Space attenuation characteristic of stress wave energy

Fig. 13 shows the variation tendency of stress wave energy with increasing propagation distance under different axial stresses. In addition, the regression results show that the stress wave energy has good exponential relations with the propagation distance (R^2=0.8968~0.9678), consistent with Eq. (6).

It is assumed that the sandstone has a uniform pore distribution under the same axial stress. Therefore, the decline rate and attenuation coefficient of the stress wave energy under different axial stresses are calculated according to Eq. (3) and Eq. (7), as shown in Fig. 14. It is found that with an increase in the axial stress, the variation tendencies of the decline rate and the attenuation coefficient underwent first a dramatic decrease, then gentle development, and finally a sharp rise. The demarcation stresses of the three stages are σ/σ_c=30%, and σ/σ_c=55%, respectively, which are consistent with Fig. 9, and Figs. 11-12. In addition, the regression analysis shows that the quadratic function can competently represent the relationships between the decline rate, the attenuation coefficient of the stress wave energy, and axial stress (R^2=0.9062, and 0.8998, respectively).

In essence, it is concluded that the changes in the decline rate and attenuation coefficient of the stress wave energy are caused by the different wave impedance of the sandstone (Jin *et al.* 2017). Also, the wave impedance can be expressed as a product of the stress wave velocity and sandstone density, which can measure the resistance of the sandstone to the energy transmission of the stress wave. Therefore, it can be inferred that with an increase in the axial stress, the wave impedance experiences three development stages, first a rapid increase, then smooth development, and finally a sharp decrease. Furthermore, its variation tendency is opposite to the decline rate and the attenuation coefficient of the stress wave energy.

The reason is that when the stress ratio, σ/σ_c was less than 30%, the decreased porosity of the sandstone results in a rapid increase in the wave impedance, and then this reduces the decline rate and attenuation coefficient of the stress wave energy. When the stress ratio, σ/σ_c is more significant than 30% and less than 55%, the sandstone porosity gradually tends to be in a stable condition, thus leading to the smooth development of the wave impedance, decline rate, and attenuation coefficient. When the stress ratio, σ/σ_c is more than 55%, as the axial stress continues to increase, the number of new pores increases rapidly and gradually dominates the development trend of the total pores in the sandstone. Therefore, the reduced wave impedance exacerbates the increasing trend of decline rate and attenuation coefficient.

4. Conclusions

In this paper, stress wave propagation tests under the same impact strength were carried out on a strip-shaped sandstone specimen using the modified SHPB. The double peak characteristics of the stress wave and the space attenuation characteristic of the stress wave energy were analyzed based on the test data, and the mathematical models were established. Some meaningful conclusions are summarized as follows.

- The presence axial stress in sandstone has a significant effect on the waveform. Only a compression wave exists and nearly no tensile wave when there is no axial stress. The compression wave and tensile wave will coexist when there is axial stress. The stress wave gradually exhibits the double peak characteristics with increasing axial stress.
- With increases in axial stress, the intensity difference of the double peak decreases exponentially and experiences first a dramatic decrease, then gentle development. The demarcation stress of the two stage is σ/σ_c=30%. The closer to the incident end of the sandstone, the faster the attenuation degree of the intensity difference. Under the same axial stress, the intensity difference decreases linearly with propagation distance, and the attenuation intensity factor k undergoes first a dramatic decrease, then smooth development, and finally a sharp increase, and its demarcation stresses are σ/σ_c=30%, σ/σ_c=55%.
- With increases in propagation distance, the time difference attenuates linearly, and the delay coefficient K undergoes first a rapid attenuation, then stable development, and finally a drastic increase. The delay coefficient K can reflect the damage evolution of sandstone.
- With increasing propagation distance, the stress wave energy attenuates exponentially, and its attenuation rate and attenuation coefficient both experience first a dramatic decrease, then gentle development, and finally a sharp increase. The quadratic function can represent the relationships between the decline rate, the attenuation coefficient of the stress wave energy, and the axial stress.

Acknowledgments

The authors would like to thank the Natural Science Basic Research Program of Shaanxi (2019JQ-762), Project funded by China Postdoctoral Science Foundation (2018M643809XB). Project Foundation of Department of Housing and Urban Rural Development of Shaanxi Province (2019-K39). We also thank LetPub (www.letpub.com) for its linguistic assistance during the preparation of this manuscript.

References

Aliabadian, Z., Sharafisafa, M., Mortazavi, A. and Maarefvand, P. (2014), "Wave and fracture propagation in continuum and faulted rock masses: Distinct element modeling", *Arab. J. Geosci.*, **7**(12), 5021-5035. https://doi.org/10.1007/s12517-013-1155-3.

Cheng, Y., Song, Z.P., Jin, J.F. and Yang, T.T. (2019), "Attenuation characteristics of stress wave peak in sandstone subjected to different axial stresses", *Adv. Mater. Sci. Eng.* https://doi.org/10.1155/2019/6320601.

Davies, E.D.H. and Hunter, S.C. (1963), "The dynamics compression testing of solids by the method of the split Hopkinson pressure bar", *J. Mech. Phys. Solids*, **11**(1), 155-179. https://doi.org/10.1016/0022-5096(63)90050-4.

Fan, L., Meng, W.N., Teng, L. and Khayat, K.H. (2020), "Effects of lightweight sand and steel fiber contents on the corrosion performance of steel rebar embedded in UHPC", *Constr. Build. Mater.*, **238**, 117709. https://doi.org/10.1016/j.conbuildmat.2019.117709.

Fan, L.F. and Sun, H.Y. (2015), "Seismic wave propagation through an in-situ stressed rock mass", *J. Appl. Geophys.*, **121**(13), 13-20. https://doi.org/10.1016/j.jappgeo.2015.07.002.

Fan, L.F., Ren, F. and Ma, G.W. (2011), "An extended displacement discontinuity method for analysis of stress wave propagation in viscoelastic rock mass", *J. Rock Mech. Geotech. Eng.*, **3**(1), 73-81. https://doi.org/10.3724/sp.j.1235.2011.00073.

Huang, M., Xu, C.S., Zhan, J.W. and Wang, J.B. (2017), "Comparative study on dynamic properties of argillaceous siltstone and its grouting-reinforced body", *Geomech. Eng.*, **13**(2), 333-352. https://doi.org/10.12989/gae.2017.13.2.333.

Jin, J.F., Cheng, Y., Chang, X.X., Yuan, W., Liang, C. and Wang, J. (2017), "Experimental study on stress wave propagation characteristics in red sandstone under axial static stress", *J. Rock Mech. Eng.*, **36**(8), 1939-1950. https://doi.org/10.13722/j.cnki.jrme.2016.1458.

Ju, Y., Sudak, L. and Xie, H.P. (2006), "Study on stress wave propagation in fractured rocks with fractal joint surfaces", *Int. J. Solids Struct.*, **44**(13), 4256-4271. https://doi.org/10.1016/j.ijsolstr.2006.11.015.

Khosravani, M.R., Nasiri, S., Anders, D. and Weinberg, K. (2019a), "Prediction of dynamic properties of ultra-high performance concrete by an artificial intelligence approach", *Adv. Eng. Softw.*, **127**, 51-58. https://doi.org/10.1016/j.advengsoft.2018.10.002.

Khosravani, M.R., Wagner, P., Frohlich, D. and Weinberg, K. (2019b), "Dynamic fracture investigations of ultra-high performance concrete by spalling tests", *Eng. Struct.*, **201**, 109844. https://doi.org/10.1016/j.engstruct.2019.109844.

Li, J.C., Ma, G.W. and Huang, X. (2010), "Analysis of wave propagation through a filled rock joint", *Rock Mech. Rock Eng.*, **43**(6), 789-798. https://doi.org/10.1007/s00603-009-0033-5.

Li, X.B., Lok, T.S. and Zhao, J. (2005), "Dynamic characteristics of granite subjected to intermediate loading rate", *Rock Mech. Rock Eng.*, **38**(1), 21-39. https://doi.org/10.1007/s00603-004-0030-7.

Lifshitz, J.M. and Leber, H. (1994), "Data processing in the split Hopkinson pressure bar tests", *Int. J. Impact Eng.*, **15**(6), 723-733. https://doi.org/10.1016/0734-743X(94)90011-9.

Nikadat, N. and Marji, M.F. (2016), "Analysis of stress distribution around tunnels by hybridized FSM and DDM considering the influences of joints parameters", *Geomech. Eng.*, **11**(2), 269-288. https://doi.org/10.12989/gae.2016.11.2.269.

Pyrak-Nolte, L.J. (1996), "The seismic response of fractures and the interrelations among fracture properties", *Int. J. Rock Mech. Min. Sci. Geomech. Abstr.*, **33**(8), 787-802. https://doi.org/10.1016/S0148-9062(96)00022-8.

Song, Z.P., Mao, J.C., Tian, X.X., Zhang, Y.W. and Wang, J.B. (2019), "Optimization analysis of controlled blasting for passing through houses at close range in super - large section tunnels", *Shock Vib.* https://doi.org/10.1155/2019/1941436.

Tian, X.X., Song, Z.P. and Wang, J.B. (2019), "Study on the propagation law of tunnel blasting vibration in stratum and blasting vibration reduction technology", *Soil Dyn. Earthq. Eng.*, **126**, 105813. https://doi.org/10.1016/j.soildyn.2019.105813.

Wang, G.S., Li, C.H., Hu, S.L. and Li, S.H. (2010), "Study on effect of contact area of structural plane on propagating properties of stress wave", *Min. Res. Develop.*, **30**(2), 50-54. https://doi.org/10.13827/j.cnki.kyyk.2010.02.011.

Wang, J., Liu, F. and Zhang, J. (2019a), "Investigation on the propagation mechanism of explosion stress wave in underground mining", *Geomech. Eng.*, **17**(3), 297-307. https://doi.org/10.12989/gae.2019.17.3.297.

Wang, T., Song Z.P., Yang J.Y., Wang, J.B. and Zhang X.G. (2019b), "Experimental research on dynamic response of red sandstone soil under impact loads", *Geomech. Eng.*, **17**(4), 393-403. https://doi.org/10.12989/gae.2019.17.4.393.

Wu, K. and Shao, Z. (2019a), "Study on the effect of flexible layer on support structures of tunnel excavated in viscoelastic rocks", *J. Eng. Mech.*, **145**(10), 04019077. https://doi.org/10.1061/(ASCE)EM.1943-7889.0001657.

Wu, K. and Shao, Z. (2019b), "Visco-elastic analysis on the effect of flexible layer on mechanical behavior of tunnels", *Int. J. Appl. Mech.*, **11**(3), 1950027. https://doi.org/10.1142/S1758825119500273.

Yoshida, S., Furuya, S. and Nishida, M. (2019), "High speed impact test on rock specimens with a compressive stress pulse". *Eng. Fract. Mech.*, **212**(S1), 132-146. https://doi.org/10.1016/j.engfracmech.2018.03.021.

GC